

MOMENTUM AND ENERGY IN THE WAKE OF A PIGEON (*COLUMBA LIVIA*) IN SLOW FLIGHT

BY G. R. SPEDDING*, J. M. V. RAYNER AND C. J. PENNYCUICK†

*Department of Zoology, University of Bristol, Woodland Road,
Bristol BS8 1UG*

Accepted 18 January 1984

SUMMARY

A technique is described whereby the vortex wake of birds in slow forward flight may be investigated with a view towards testing some of the assumptions and predictions of existing theoretical models of bird flight. Multiflash stereophotogrammetry was used to analyse the wake as a pigeon passed through a cloud of neutrally-buoyant helium bubbles.

All photographs obtained support the hypothesis that the wake is composed of a chain of discrete, small-cored vortex rings. This being the case, velocity profiles taken from sections through the wake allow us to estimate the momentum in the wake as represented by vortex rings.

The momentum in the wake appears to be approximately half that required for weight support in unaccelerated, level flight. The possible causes and consequences of this paradoxical result are discussed.

INTRODUCTION

Theoretical models purporting to predict the power output of flying birds have become increasingly elaborate over the years (e.g. Pennycuick, 1975; Rayner, 1979*a,b*), but confidence in their predictive value remains limited, owing to the difficulty of testing the predictions. Tucker (1973) found a promising degree of agreement between predictions based on mechanical analyses and measurements of oxygen consumption. However, the comparison cannot be carried to a high degree of detail because the physiological measurements do not allow different components of the power requirements to be discriminated. The measurement of oxygen consumption yields a single value, which, according to mechanical theory, is made up from several components, including induced, parasite and profile power components. Where the measured and predicted results differ, it is difficult to tell whether the discrepancy is due to an error in prediction of one or several components of power or to a flaw in the underlying concept of additive power components. Furthermore, chemical power, as reflected in oxygen consumption, is converted into mechanical power with an unknown efficiency, which may or may not itself be independent of speed or power.

* Present address: Department of Aerospace Engineering, University of Southern California, Los Angeles, California 90089-1454, U.S.A.

† Present address: Department of Biology, University of Miami, P.O. Box 249118, Coral Gables, Florida 33124, U.S.A.

■ Key words: Bird flight, vortex wake, induced power.

This paper describes an attempt to single out one component of power, the induced power, and to measure it independently of the rest. The induced power is that which is expended in supporting the bird's weight. In level flight, the weight must be balanced by a force equal to the rate at which momentum is imparted to the air. The induced power is the rate at which the bird imparts kinetic energy to the air in order to create the necessary momentum. It should be possible to examine the wake after the bird has passed, and measure the kinetic energy left behind.

In principle, this could be done without making any prior assumptions about the structure of the wake. However, it is much easier to estimate momentum and energy in relation to a specific model of the structure expected in the wake. The vortex ring model of the wake, developed by Rayner (1979*a,b*) was used as a basis for the analysis. If the wake does indeed consist of vortex rings as predicted, it should be a simple matter to calculate the energy of each ring, and hence the induced power.

The first objective was to ascertain whether vortex rings with the predicted characteristics occur. Having confirmed this, the next objective was to make a semi-independent estimate of the wake energy and hence the induced power requirement. These can then be compared with the predictions of the vortex-ring model.

METHODS

Pigeon training

Three pigeons (*Columba livia* Gm) were trained to fly in response to the alternate switching of two red lights. The naïve bird was introduced at one end of a flight cage (dimensions $4 \times 2.7 \times 1.2$ m, Fig. 1) with a red light illuminated at that end. When the bird's attention appeared to be directed down the length of the cage, the lights were switched and about 0.5 s later a small disturbance created behind the bird would induce it to fly to the illuminated bulb at the other end of the flight cage. After a calming period of 10–20 s the procedure was repeated. Training sessions typically lasted 30–60 min and were repeated daily for 2–4 weeks after which the pigeons would fly in response to the light switching without any other cues. Training continued in reduced light levels and in conditions gradually approaching those of the experiment. After 10 weeks, one pigeon had been trained to the point where level and repeatable flights could be evoked at the flick of a switch. Flights were repeated under 4 kW of light and filmed at $200 \text{ frames s}^{-1}$ with a Photosonics IPL high speed ciné-camera. Analysis of these films revealed no significant accelerations of the body and no measurable departure from horizontal motion in the test section of the flight cage. The morphology and kinematics measured directly and by film analysis respectively are given in Table 1.

Helium bubbles

A cloud of neutrally-buoyant helium bubbles (approx. 3 mm diameter) was generated by an Armfield SAI Bubble Generator with a low-speed head (No. 2). Helium, air and bubble film solution were passed at carefully metered flow rates to a mixing head where bubbles were produced at the tip of three concentric tubes. The design, construction and development of a helium bubble flow visualization system

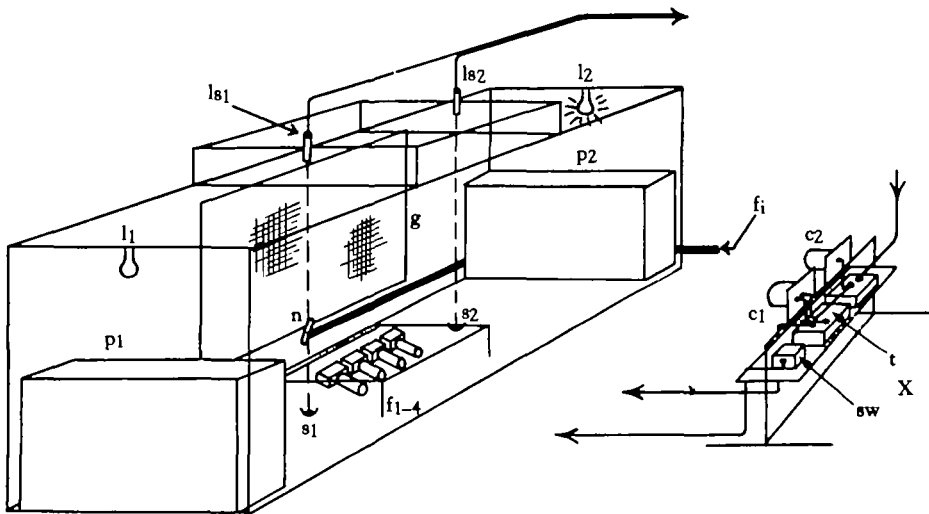


Fig. 1. The flight cage, camera, lighting and bubble generation systems. Metered flow rates of helium, air and soap solution are provided at f_1 to form the helium bubbles at exit nozzle, n . Flashguns f_{1-4} rest pointing upwards and slightly away from the background grid, g , to maximize contrast, and are covered by a Perspex lid. The pigeon flies straight between platforms p_1 and p_2 , which are both 1.5 m from the floor, according to the switching of lights l_1 and l_2 . In mid-flight, the pigeon interrupts the focused infra-red light beams from s_1 , s_2 to trigger dark-activated switches ls_1 , ls_2 . According to the direction of flight, one of these switches opens the shutters of the cameras c_1 , c_2 . These, in turn start the flash timer, t , triggering the sequence of flashguns, f_{1-4} . After approximately 2 weeks training of the pigeons, the centre of the front face of the wire mesh cage could be safely removed. The experimenter, standing at X , effectively controls the entire operation when switching between l_1 and l_2 with sw .

Table 1. *Kinematics and morphology of the pigeon used in flight cage experiments*

Parameter	Symbol	Units	Value
Body mass	M	kg	0.350
Wing semi-span	b	m	0.33
Wing area	S	m^2	0.062
Flight velocity	V	$m\ s^{-1}$	2.4
Wingbeat frequency	f	s^{-1}	6.67
Stroke period	T	s	0.15
Downstroke period	T_d	s	0.067
Upstroke period	T_u	s	0.083
Downstroke ratio	τ		0.45
Stroke plane angle	γ	degrees	55
Stroke amplitude	ϕ	degrees	150
Body tilt	β	degrees	35

Kinematics measured from high-speed film.

have been described by Lee (1976). The bubble generator head was positioned 0.35 m from the floor and tilted at 30° from the vertical back wall of the flight cage to produce a cloud of bubbles with low initial velocity in the field of view of the camera system.

Photography

Two motor-driven Nikon cameras (F2 and FM) with micro-Nikkor 55 mm (f3.5) lenses were mounted on wooden blocks on a rigid frame of slotted steel angle. The lens

centres were separated by a horizontal distance of 0.25 m and the wooden mounting blocks were filed down so that the lenses were at the same height, as measured with a steel rule (± 0.2 mm). A plumb line was used to fix a planar, vertical, background grid (2 cm squares in a 2.45×1.22 m area) along the back wall of the flight cage, and camera orientation normal to the grid was checked by sighting down the lenses at a mirror mounted flush with the grid surface.

Four Sunpak AZ5000 flashguns (GN48 at 100 ASA) were mounted at a small angle to the floor of the flight cage to maximize contrast between the bubbles and the background. The flashguns were triggered sequentially at intervals determined by a chain of four 555 timers. Opto-isolators before the SCRs in each timing circuit prevented interference from the high voltage switching of the flashguns. Time interval settings were calibrated with a Marconi Instruments Universal Counter Timer 2438 applied at the opto-isolator output pins. With the flashguns set at full power, the photographic depth of field spanned the entire width of the flight cage, and the gradual tail-off in light intensity (total flash duration approx. 3.5 ms) of each flash allowed the direction of travel of each bubble to be deduced.

In the experiments, the camera shutters were opened for $1/8$ s, during which time the four flashguns were triggered; camera apertures were set at f32. Ilford HP5 film was processed in Acuspeed developer at an equivalent speed of 800 ASA and the negatives were then printed with a Leitz Focomat V35 enlarger and 40 mm Zeiss lens onto 18×24 cm sheets of Kodalith 4556 or Ilfolith IH7 lithographic film. These positive enlarged transparencies formed the raw material for all subsequent analysis.

Photogrammetry

In this section we briefly describe how the photocoordinates (x, y) of bubble images on pairs of stereophotographs (stereopairs) were used to derive their three-dimensional real space coordinates (X, Y, Z). The object space is that part of real space containing information to be used in the analysis. An exposure station is the position of the camera at the time of exposure, or more precisely in this case, the location of the point half-way between the incident nodal point and the emergent nodal point along the optical axis of the lens. This 'lens centre' was estimated from technical drawings supplied by Nikon. The principal point on a photograph is that point at the intersection of the focal plane with a line from the rear nodal point of the camera lens perpendicular to the focal plane.

The two enlarged lith positives of a stereopair were fixed on the carriages of a Karl Zeiss Jena Stecometer (stereocomparator) where corresponding points on the stereopair could be measured. The photographs were viewed in stereo through binoculars and their positions, absolute and relative, were adjusted until a reference floating mark appeared to rest on the desired point. At the push of a button, the stereocomparator coordinates (\bar{x}, \bar{y}) of the left and right photographs were recorded. For each stereopair, up to 2500 bubble images were digitized in this fashion and recorded on paper tape.

For each stereopair, the four corner points of the left and right photographs were digitized so that the data in the stereocomparator coordinate system could be converted to a photographic coordinate system with origin at the principal point, if the principal point was assumed to lie at the intersection of the diagonal lines joining opposite corner points. This is illustrated in Fig. 2A, where the comparator coordinates of the

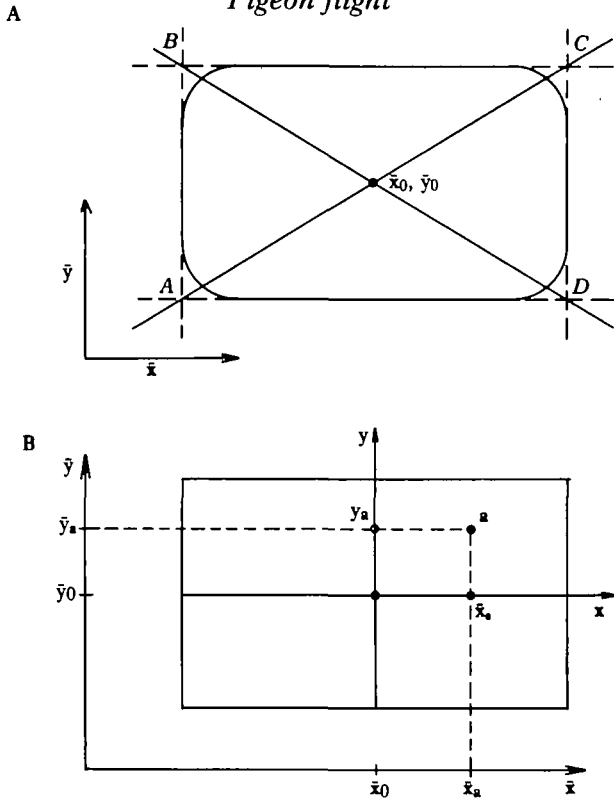


Fig. 2. (A) The principal point (\bar{x}_0, \bar{y}_0) marks the intersection of principal rays from the perspective centre with the negative after they have travelled through the lens system. In a first estimate, it is assumed to lie in the geometric centre of the negative frame. Under magnification, the corners of the frame are actually curved (exaggerated in this diagram) and the corner points are taken from linear extrapolation of the frame edges. (B) All data points in the stereocomparator coordinate system (\bar{x}, \bar{y}) are now expressed in a photographic coordinate system (x, y) with origin at the principal point.

principal point (\bar{x}_0, \bar{y}_0) are calculated from the comparator coordinates of the corner points of the photograph $(\bar{x}_{A-D}, \bar{y}_{A-D})$ by

$$\bar{x}_0 = \frac{1}{4} (\bar{x}_A + \bar{x}_B + \bar{x}_C + \bar{x}_D), \quad (1)$$

and

$$\bar{y}_0 = \frac{1}{4} (\bar{y}_A + \bar{y}_B + \bar{y}_C + \bar{y}_D).$$

The comparator coordinates (\bar{x}, \bar{y}) of a point may now be reduced to photocoordinates (x, y) with origin at the principal point by the simple relation:

$$\begin{aligned} x &= \bar{x} - \bar{x}_0, \\ y &= \bar{y} - \bar{y}_0, \end{aligned} \quad (2)$$

as shown in Fig. 2B. The relationship between these photocoordinates (x, y) and the object space coordinates (X, Y, Z) for any given point is simple and exact if certain conditions are satisfied. The basic geometry is given in Fig. 3. The point A has object space coordinates X_A, Y_A, Z_A and its image has photocoordinates (x'_a, y'_a) and (x_a, y_a) the left and right photographs respectively. The horizontal distance between

exposure stations L_1 and L_2 is the camera base B . B is parallel to the X axis and is at distance H from it along the Z axis which runs parallel to the optical axes of the camera lenses. f is the focal length of the lenses. The position of A in object space is related to the *parallax* of that point. For the geometry considered here, only x -parallax occurs and this change in x coordinate from one photograph to the next is simply,

$$p_a = x_a - x'_a. \quad (3)$$

X_A , Y_A and Z_A are now given by the parallax equations which may be derived by considering similar triangles in Fig. 3,

$$X_A = B \left(\frac{x_a}{p_a} \right),$$

$$Y_A = B \left(\frac{y_a}{p_a} \right),$$

and
$$Z_A = H - B \left(\frac{f}{p_a} \right). \quad (4)$$

In equations (4), x_a , y_a and p_a have been measured from the photographs, H and B are known and f is known, at least nominally. Equations (1)–(4) were applied to each point in object space (i.e. to each bubble image) to yield real space coordinates which were then corrected for systematic errors as described in the next section. All photogrammetric details herein, including Fig. 3, are adapted from Wolf (1974). A clear derivation of the parallax equations may be found in Hallert (1960) and Thompson (1966) contains a thorough discussion on the sources of errors and their correction.

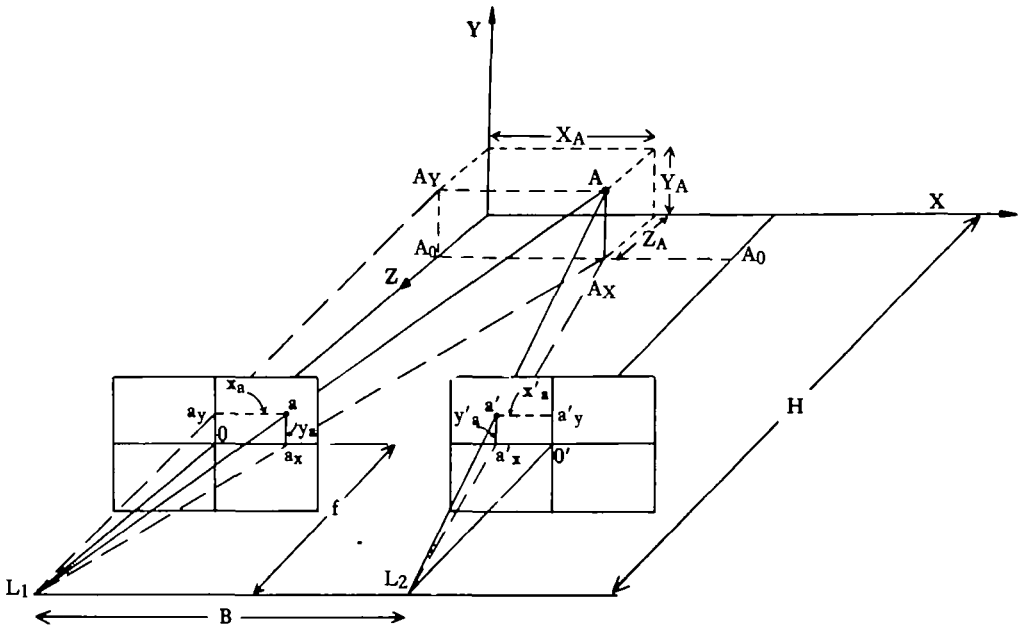


Fig. 3. Perspective geometry of a pair of normally orientated overlapping photographs. The point A in object space appears at a and a' in the left and right photographs respectively.

Sources of error

As can be seen in Fig. 3, the parallax equations assume that the cameras are aligned with their lens axes parallel to each other and normal to the ground base plane XY. Errors in the determination of H and B enter directly into equations (4). H could be fixed to ± 0.5 mm ($1/6 \times$ mean bubble diameter) and B was determined to within 0.2 mm. The focal length is also assumed to be fixed and affects the scaling in Z, although it is in fact known only nominally from lens specifications. As measurements have been taken from enlarged positives, scaling corrections must be applied later from analysis of a control object of known dimensions, and these will also take care of any uncertainty in the focal length. The accuracy of the measured photocoordinates (x_a, y_a) and the parallax between them, p_a , is affected by any deviation from the ideal geometry of Fig. 3. Errors in the determination of the principal point, lens aberrations, film emulsion shrinkage, film curvature in the camera or enlarger and imprecise orientation of the photographic system will all affect the fidelity of the final result.

Corrections

The lack of geometric stability may be compensated for, given sufficient object space control and an analytical data reduction system (Karara & Faig, 1980). Specialized techniques requiring extensive object space control (reviewed by Karara, 1980) cannot be used here as the flight path must remain free of obstructions. We make use of the fact that the camera positions are accurately determined so that they themselves may be used as control points in object space. Also, taking advantage of the fact that the data points are well distributed in space, the data field can be subdivided into a number of separate blocks where the small distortions are corrected by applying the technique known to photogrammetrists as 'relative orientation by collinearity' (Faig, 1973). Here, a set of collinearity equations are written for each point in object space, expressing the ideal condition that the exposure station, an object point and its photographic image all lie on a straight line. So,

$$\begin{aligned} x_a &= -f \left[\frac{m_{11}(X_A - X_L) + m_{12}(Y_A - Y_L) + m_{13}(Z_A - Z_L)}{m_{31}(X_A - X_L) + m_{32}(Y_A - Y_L) + m_{33}(Z_A - Z_L)} \right], \\ \text{and} \quad y_a &= -f \left[\frac{m_{21}(X_A - X_L) + m_{22}(Y_A - Y_L) + m_{23}(Z_A - Z_L)}{m_{31}(X_A - X_L) + m_{32}(Y_A - Y_L) + m_{33}(Z_A - Z_L)} \right], \end{aligned} \quad (5)$$

where x_a and y_a are the photocoordinates of an image point with real space coordinates X_A, Y_A, Z_A . The exposure station has real space coordinates X_L, Y_L, Z_L , f is the focal length of the camera and the m coefficients are functions of the rotation angles ω , ϕ and κ about X, Y and Z respectively, known as the direction cosines. The equations are linearized by taking the first terms of a Taylor series and solving iteratively to a preset convergence limit. Again, these equations may be found in Wolf (1974) and are thoroughly derived with examples of applications by Inghilleri (1968). When there are more than five object points, some data are redundant and a least squares solution is used, resulting in corrected real space coordinates for each point, together with statistics concerning residual errors and standard deviations for position estimates of each point.

Scaling in X, Y and Z is calculated by reference to stereopairs of a control cube analysed in the same way. A cube with sides of 0.2 m was suspended in object space and photographed and scaling factors were determined by the apparent lengths of X, Y and Z in the reconstructed image. The cameras were not moved after this calibration procedure. Subsequent reconstruction of the same cube from another stereopair produced mean standard deviations of 0.35 mm in X, 0.33 mm in Y and 0.52 mm in Z. The mean difference between measured and calculated lengths on the cube was ± 0.50 mm. Given an estimate for the standard deviation of each time interval from timer calibration, the standard error of velocity measurements may be calculated (G. M. Jarman, personal communication), and measured velocities should be accurate to within 10 %.

Construction of velocity maps

The u, v and w components of velocity in X, Y and Z respectively were calculated over each of the three time intervals within each set of four bubble images. Velocity maps were drawn by plotting the particle paths in two dimensions and the length of these lines are directly proportional to the velocity in that plane. When it proved convenient to refer bubble movements and velocities to some other system of rotated coordinates, the following rotation equations were applied:

$$\begin{aligned} X' &= X\cos\kappa + Y\sin\kappa \\ Y' &= Y\cos\kappa - X\sin\kappa. \end{aligned} \quad (6)$$

Rotation about the Z axis through an angle κ transforms the original X, Y coordinates to X', Y'. Bubble velocities are then recalculated for this system as before. Sections could be taken through the bubble field in any plane, taking slices thin enough so that three dimensional effects may be regarded as being constant across that slice.

Analysis and computer facilities

Paper tape issuing from the stereocomparator was fed to the Honeywell Multics Computer System at the University of Bristol where all photogrammetric analysis and velocity field calculations were performed. All programmes were written in FORTRAN IV; that used for relative orientation was adapted from code written by P. R. Wolf. All model calculations which are discussed later in this paper were performed on a Research Machines 380Z microcomputer in Microsoft BASIC and ciné-film analysis was performed on a NAC Film Motion Analyser connected to the same machine.

RESULTS

Wake structure and velocity profiles

Fig. 4 is typical of the approximately 900 stereopairs obtained which indicate that a ring-like structure does exist in the wake. We may note that the helium bubbles appear to be following the air flow faithfully.

In 210 of these stereopairs, conditions were determined accurately enough for quantitative work. Owing to the large number of computer and man hours required

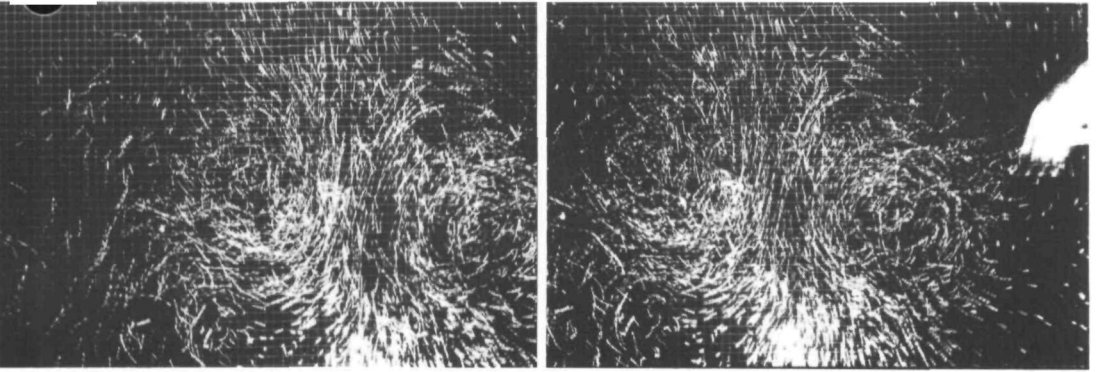


Fig. 4. The vortex wake of a pigeon in horizontal flight at 2.4 m s^{-1} . The pigeon, flying from left to right across the field of view leaves a vortex ring structure in the wake, as shown by the multiple images of the helium bubbles. Each bubble reflects light off both the front and back surfaces of the soap film and so appears as a double streak line. The mean time between successive images is 5 ms. The squares in the grid are $2 \text{ cm} \times 2 \text{ cm}$.

Only five stereopairs were fully analysed. The selection criteria were that there should be an extensive but well distributed coverage of bubbles in the wake and that the wake structure produced during one wingbeat cycle (downstroke + upstroke) should be visible in stereo. After inspecting 900 stereopairs, the development and general structure of the wake are quite familiar and readily identified. The following results are outlined with reference to one representative stereopair. The consistency of the wake parameters measured in all five stereopairs and summarized in Table 2 is thought to justify such an approach.

Figs 5 and 6 are simple reconstructions of the wake. The pigeon flew from right to left across the field of view and the multiple exposure of the tail has been outlined in Fig. 5A. There are 1828 bubble images represented here, most of them in the foreground, as stereo views of bubbles far from the cameras were often obscured or confused by the intervening bubble cloud. The wingbeat is assumed to be symmetrical about the mid-plane and the wake is also taken to be symmetrical about the same plane. In the plan view of Fig. 5B the position of the outspread tail feathers is shown together with a scale bar showing the extent of the wingspan. The same format is shown in Fig. 6 which shows four vertical slices, 100 mm thick, in sections 1–4 moving from the background towards the cameras. Sections 1 and 2 straddle the mid-plane and sections 3 and 4 cut through the outer regions of a ring-like structure. The general wake structure revealed is similar to that which might be expected for sections through a small-cored vortex ring. The hypothesis that such a ring is present may be further tested by constructing velocity profiles for various sections through the wake; these may be compared with those reported in experimental studies of vortex rings by Sullivan, Widnall & Ezekiel (1973), Sallet & Widmayer (1974), Didden (1977), Maxworthy (1977) and Gühler & Sallet (1979), among others. Fig. 7 shows the coordinate systems and notation used in this study. Note that the vortex structures in the wake are generally inclined from the horizontal, the angle ψ being the angle between the horizontal and a convenient longitudinal axis in the wake. This corresponds to the ring momentum angle of Rayner (1979a) for a wake composed of vortex rings. Note also that experiments were conducted with the bird flying both from left to right (Fig. 4) and from right to left across the field of view (Figs 5, 6, 7). This causes few problems in the analysis, the major change being the change in sign of ψ . There is some asymmetry in the wake however (cf. Fig. 8) which will be discussed later and all following analysis and discussion assumes the bird to be flying from right to left.

The $v(X')$ velocity profile of Fig. 8 shows the variation in fluid velocity normal to the ring plane as we move along the ring plane at the centre line Z_0 . $v(X')$ profiles were obtained for a series of sections over the whole range of Z and conformed to expected flow patterns for sections across a vortex ring. At the midline, Z_0 , dv/dX' is greatest as v changes sign across the vortex core. Remembering that Fig. 8 is a superposition of the circulatory flow of the vortex together with its own translational motion (the

Fig. 5. Reconstructions of the three dimensional bubble field. (A) Projected onto the XY plane and viewed from along the Z axis. The leading bubble (the final image in the series of four) is plotted as a circle and the length of the trailing 'tail' is proportional to the magnitude of the velocity in XY. The angle between the estimated ring plane and the horizontal is the ring momentum angle, ψ . (B) Projection onto the Z plane, viewed from along the Y axis. Format as in (A). The pigeon's tail position and wing span ($2b = 0.66$ m) are shown.

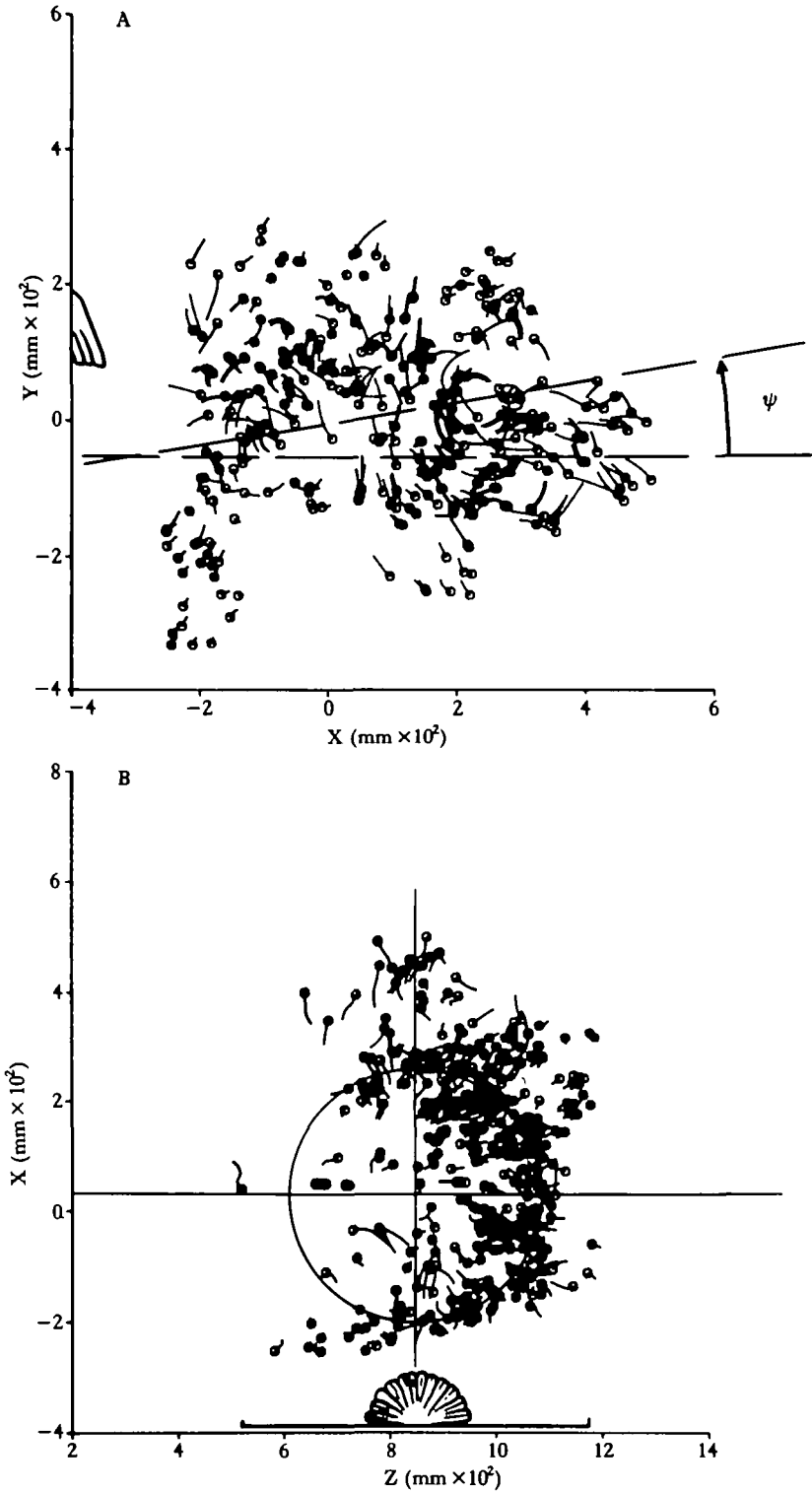


Fig. 5

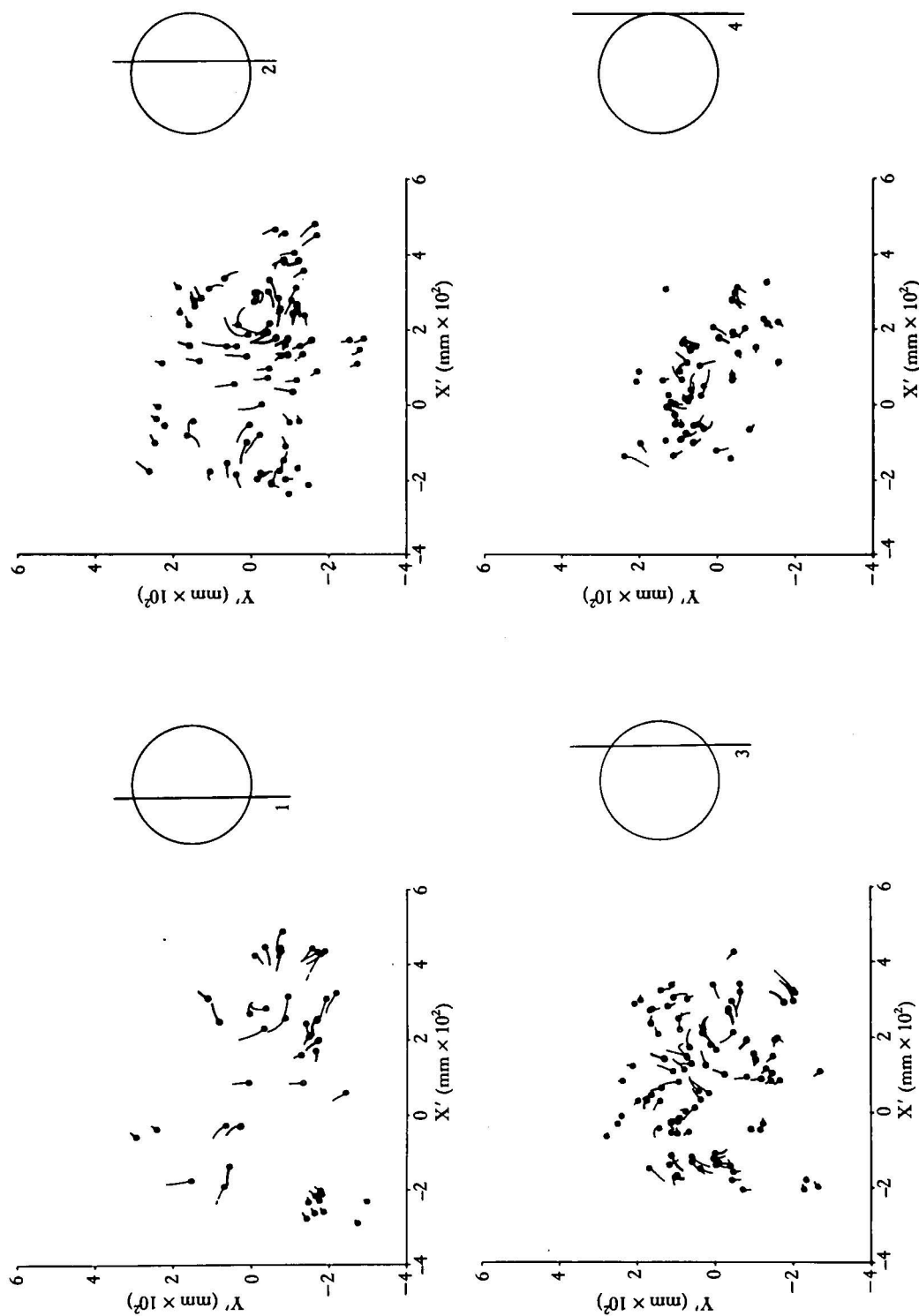


Fig. 6. Four vertical sections taken through the bubble field showing bubble velocities in the plane of the section. The coordinate system (X' , Y') has been rotated through the angle ψ about Z . Sections are taken at positions 1–4 through the ring-like wake structures.

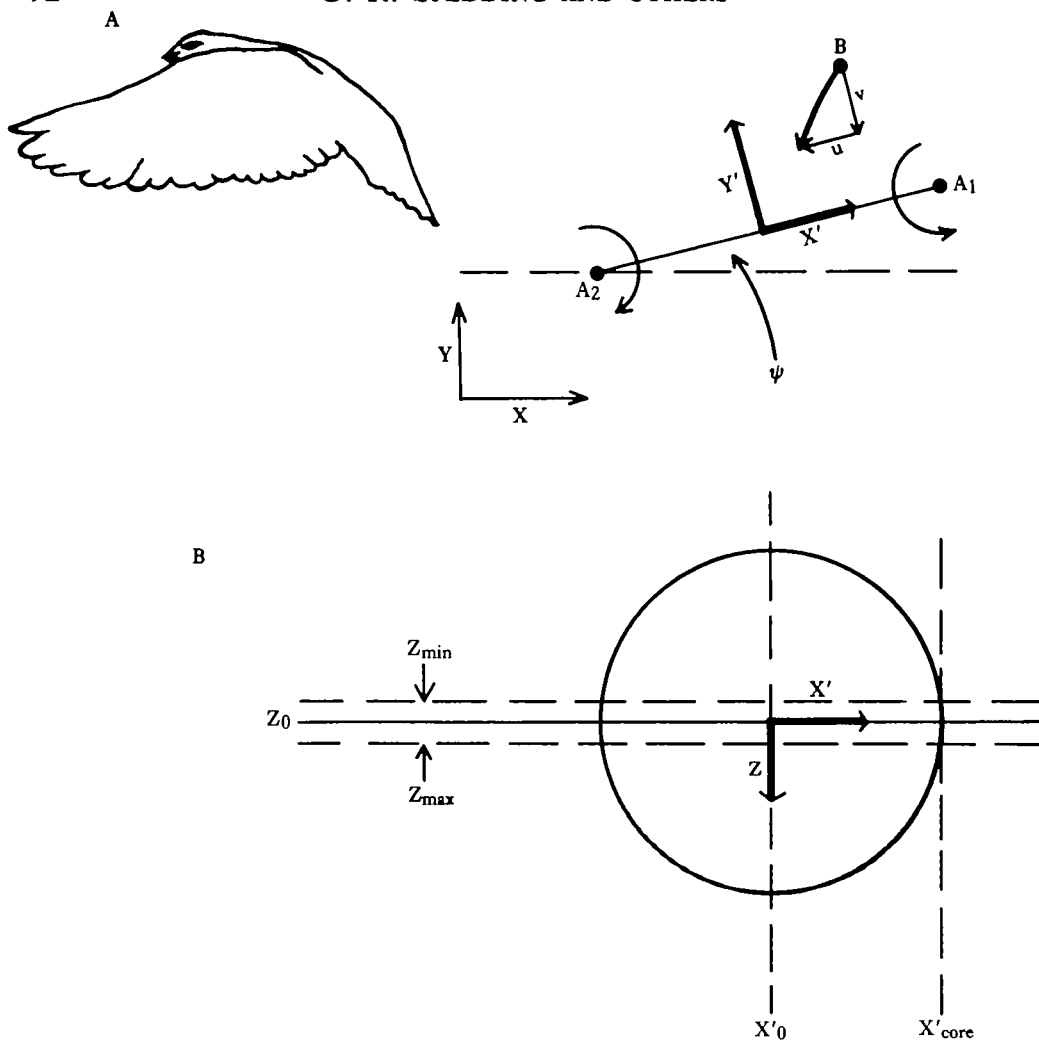


Fig. 7. Coordinate systems and notation. (A) The origin of the XY coordinates is arbitrarily set at the left camera lens centre. The X', Y', Z system is defined relative to the wake structure, seen here in cross section with cross-sections of a vortex at A_1 and A_2 . The motion of the bubble is resolved into u and v components along X' and Y' respectively. ψ is the ring momentum angle. (B) Plan view from along the Y' axis. X'_{core} is the X' coordinate of the centre of the vortex core. Velocity profiles in Figs 8, 9 and 11 are confined to a small range of Z about Z_0 .

ring is convecting downwards away from the bird), the vortex core location is given by the intersection of the line of $v(X')$ with a horizontal line at U_s , the ring convection velocity. U_s is a mean value taken by measuring the distance between successive rings on photographs where this could be discerned; there were 32 of these. The distance travelled by one ring during one stroke period (T) could be calculated, T is known from ciné-film analysis, and U_s was thus estimated at 1.25 m s^{-1} , s.d. 0.3. This value is marked on the v axis of Fig. 8. We note that the slope of $v(X')$ is not symmetrical about X'_0 . The steeper, better defined slope on the right of the figure corresponds to the starting vortex shed by the wings while the left-hand side of the curve intersects the stopping vortex produced at the end of the downstroke. In an ideal vortex ring

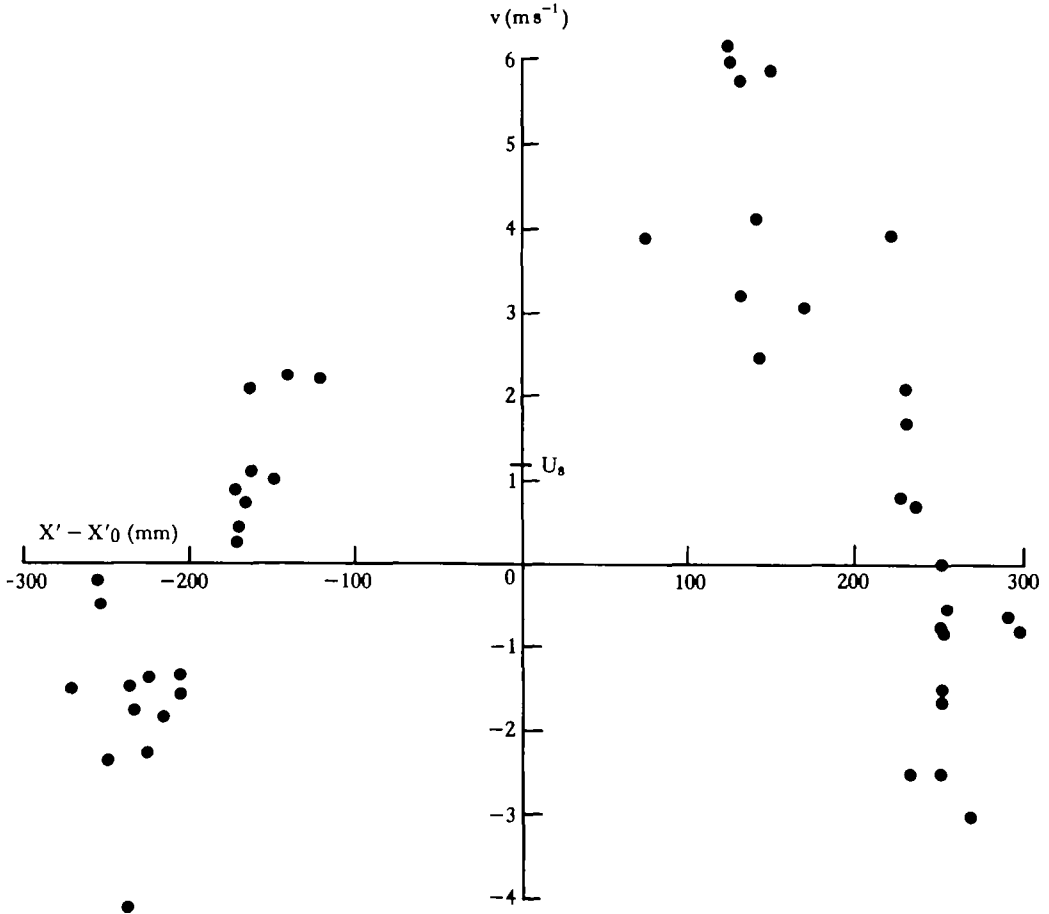


Fig. 8. $v(X')$ for a small range of Z about Z_0 and Y' about Y'_0 . v is positive when the flow is downward, as defined in Fig. 7.

these two cross-sections would be identical. The departure from this condition, which can be seen on close inspection of many stereopairs, is small but consistent. It is not obvious whether this might be due to distortion by the next ring in the chain, incomplete roll-up of the more recently shed wake vorticity or if it reflects a time history of wing circulation and hence vortex shedding into the wake which precludes the formation of a truly axisymmetric vortex ring. During the course of this investigation we found that each ring was affected by the development of the next ring in the chain, indicated by an increase in the ring momentum angle ψ with time which was pronounced on the downstroke producing the newest vortex ring. Of the choices outlined above, the first thus seems to be implied, but in the absence of any further evidence we note that the effect is small, ignore it, and concentrate on the velocity profiles across the right-hand vortex core which is less distorted by interaction with other wake elements.

Having thus located the core position in X' , X'_{core} , a profile of $u(Y')$ may be taken where the velocity parallel to the ring plane is plotted along a line running normal to the ring plane, through the vortex core, centred at Z_0 . The resulting profile of Fig. 9 has the expected shape as u reaches peak values $\pm u_{\text{max}}$ at the edge of the vortex core, decaying

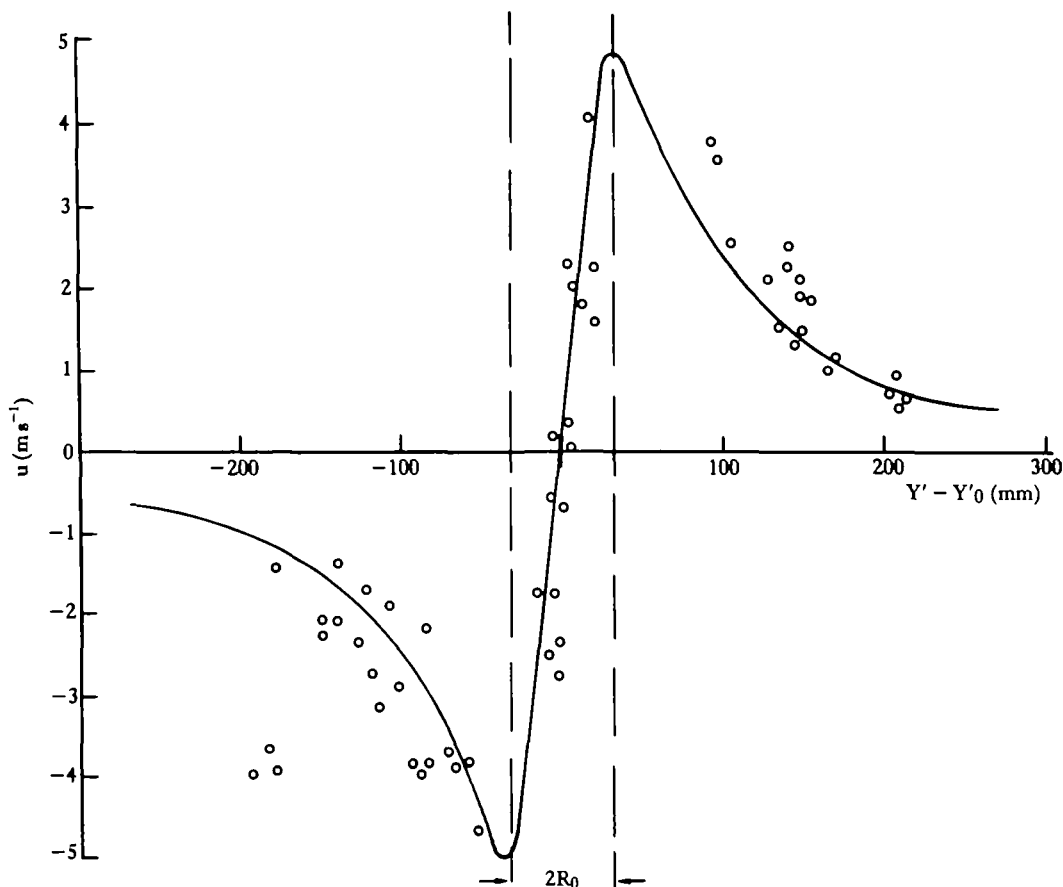


Fig. 9. $u(Y')$ around Z_0 and X'_{core} .

thereafter with $|Y' - Y'_0|$. The diameter of the vortex core is given by the distance in Y' between u_{\min} and u_{\max} . The curve has been fitted by eye and this, together with the scatter in the data, lends some uncertainty to the value of R_0 . However, this did take into account information from neighbouring profiles at different Z locations and the fact that each section has a finite thickness when a least squares best fit would always underestimate u_{\min} , u_{\max} and du/dY' and similarly overestimate R_0 , to an extent depending on the thickness of the section. A conservative error estimate would be $\pm 20\%$ which is close to the standard deviation for all measurements (Table 2).

From such data as presented in Figs 8 and 9, the vorticity ω can be calculated at Z_0 where the vorticity component due to a vortex line parallel to the Z axis is defined (e.g. Batchelor, 1967) by

$$\omega = \frac{\partial u}{\partial Y'} - \frac{\partial v}{\partial X'}. \quad (7)$$

The distribution of vorticity across the vortex core is given in Fig. 10. $\partial u/\partial Y'$ and $-\partial v/\partial X'$ were taken from smoothed curves fitted to the $v(X')$ and $u(Y')$ velocity

profiles. These points are plotted in Fig. 10 and a smooth curve is drawn through ω which is the sum of the two. While ω appears to be confined largely to within the vortex core as defined in Fig. 9 by u_{\max} , the resolution of the technique cannot be claimed to be fine enough to justify any more precise description.

The circulation, K , a measure of the total vortex strength, is defined by the line integral of the fluid velocity round any closed curve surrounding the vortex (Batchelor,

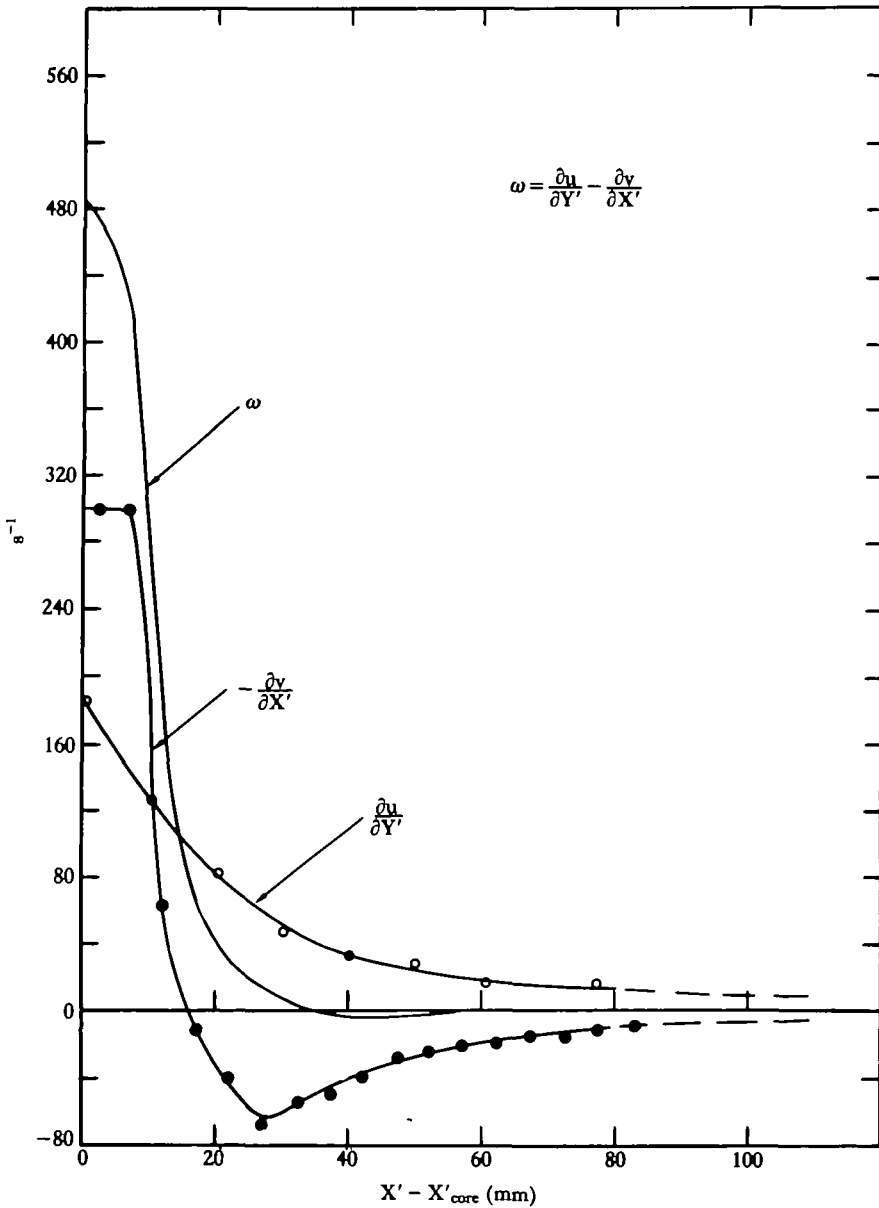


Fig. 10. The vorticity distribution $\omega(X' - X'_{\text{core}})$ across the vortex core.

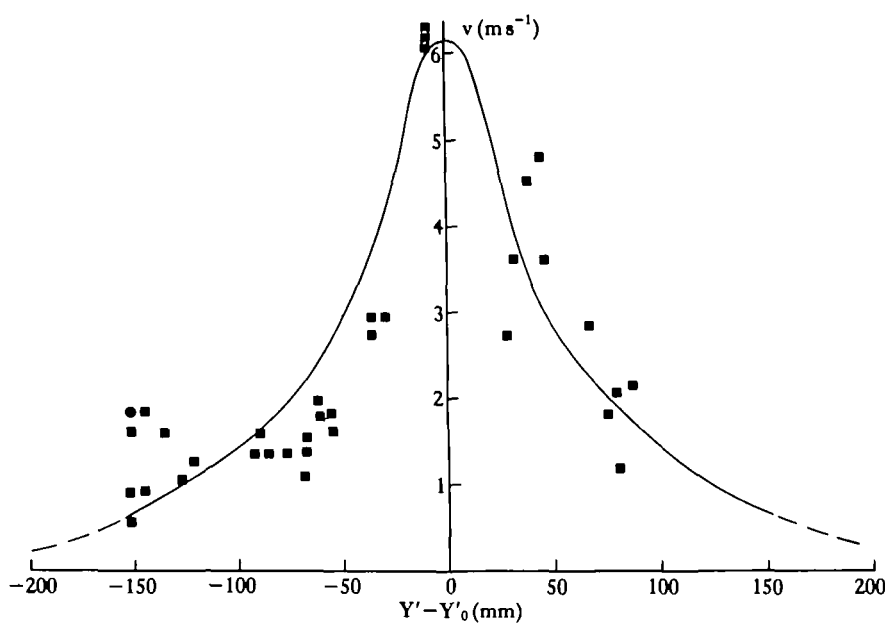


Fig. 11. $v(Y')$ around Z_0 and X'_0 . This curve is integrated to estimate the circulation K .

1967) and following the previous experimental investigations mentioned we calculate it from

$$K = \int_{-\infty}^{+\infty} v \cdot dY'. \tag{8}$$

The curve of the fluid velocity normal to the ring along a line running normal to the ring plane and along the axis of symmetry is shown in Fig. 11. This curve of $v(Y')$ at X'_0 has been drawn by eye, reflecting the fact that data in this region are somewhat sparse as bubbles moving at high velocity in a straight or nearly straight path were difficult to identify without ambiguity. Further from the ring plane, slowly moving bubbles, appearing as a blur of closely-superimposed images, were also impossible to digitize accurately. We integrate under this line assuming symmetry about the ring plane and a rapid decay of v in the far field. This is confirmed in the photographs. The uncertainty in this estimate of K should be $\pm 20\%$ at the outside.

Table 2. *Wake parameters measured from five stereopairs*

Ring parameter	Units	Stereopair number					Mean	s.d.
		P1	P2	P3	P4	P5		
Momentum angle, ψ	degrees	8.0	13.5	13.0	9.0	10.5	10.8	2.4
Ring length	m	0.424	0.396	0.452	0.397	0.400	0.414	0.024
Ring width	m	0.400	0.381	0.442	0.390	0.386	0.400	0.025
Core radius, R_0	m	0.031	0.046	0.034	0.030	0.034	0.035	0.006
R_0/R		0.15	0.24	0.16	0.15	0.17	0.17	0.038
Circulation, K	$m^2 s^{-1}$	1.52	1.80	1.66	2.08	1.55	1.72	0.23

In all cases, velocity profiles obtained from sections through the wake were consistent with the hypothesis that it is composed of vortex rings. The results are summarized in Table 2.

Vortex ring energy

A direct estimate of the self-energy of these vortex rings can now be made if the ring is assumed to be circular. As Table 2 shows, the ratio of the vortex core radius R_0 to the vortex ring radius R is small. Fraenkel (1970), Saffman (1970) and Norbury (1973) have demonstrated that when R_0/R is less than 0.25, the self-energy of a small-cored, planar, circular vortex ring is given by the formula:

$$E_s = \frac{1}{2} \rho K^2 R [\ln(8R/R_0) + \bar{A} - 2]. \quad (9)$$

As an isolated circular vortex ring persists without deformation, this kinetic energy will remain constant as the ring travels. The presence of vorticity elsewhere in the flow field (including on the wings) can induce deformation in the ring under investigation, but the instantaneous self-energy can still be derived from equation (9). There are additional energy components resulting from vortex interactions (mutual energy), but experience with the vortex ring model (Rayner, 1979a,b) has shown that these interactions are probably small compared to the self-energy. Moreover, the most obvious effect of such interactions is a perturbation to the convection velocity U_∞ , and as such it is already accounted by this experimental method. In these experiments, the circulation K and ring dimensions R and R_0 have all been measured, the air density ρ is known to be 1.205 kg m^{-3} at 20°C , and it remains to assign a value to the constant \bar{A} . \bar{A} varies between 0 and 0.5, depending on the distribution of vorticity ω across the vortex core, and has the value 0.25 when the vorticity is constant across the core. Although Fig. 10 shows that ω declines a little towards the edge of the core, 0.25 has been chosen here for ease of comparison with the vortex ring model. The calculated value of E_s for each stereopair appears in Table 3.

Model predictions

The vortex ring model (Rayner, 1979a,b) used here for comparison with experiment is based on the logic that in steady level flight the mean forces acting on the bird are in equilibrium. The vortex-based forces of lift and induced drag must balance weight and the frictional drag forces. If it is assumed that useful aerodynamic force is generated by the downstroke alone, then momentum to support and propel the bird is transferred to the wake in the form of discrete bursts of vorticity, each representing a single downstroke. By the laws of vortex conservation these bursts must be composed of closed vortex loops, and it is natural to choose to model these structures as small-cored vortex rings. As pointed out by Lighthill (1973), a vortex ring has the property of conveying a given quantity of momentum with the least energy (or induced drag), and is therefore likely to be selected by birds – if feasible – since power economy in flight is critical. It is well known that subsonic aircraft wakes roll up into small-cored line vortices, and there is limited previous experimental evidence (Magnan, Perrilliat-Botonet & Girerd, 1938; Kokshaysky, 1979) that, in some birds at least, the wake of a flapping wing consists of discrete vortex rings. The experiments described here provide further strong evidence for this hypothesis, and give the first

Table 3. *Comparison of wake parameters as predicted by the vortex-ring model (left) and as measured by experiment (right)*

	Model predictions	Measured
Ring dimensions: long axis (m)	0.557	0.414
short axis (m)	0.495	0.400
ring radius R (m)	0.263	0.203
core radius R_0 (m)	0.045	0.035
R_0/R	0.17	0.17
Ring momentum angle ψ (degrees)	0.30	10.8
Wake element spacings		
normal to the ring plane	0.324	0.221
parallel to ring plane	0.360	0.336
Ring convection velocity U_s (m s^{-1})	2.15	1.25
Ring circulation K ($\text{m}^2 \text{s}^{-1}$)	1.97	1.72
Ring momentum $\rho K \pi R^2$ ($\text{kg m}^{-1} \text{s}^{-1}$)	0.514*	0.270
Ring self-energy E_s (J)	1.29	0.76
Induced power (W)	9.56	5.05

In both cases ring radius R is the geometric mean of the long and short semi-axes; in the model predictions, relative core radius R_0/R has been set to the measured value 0.17.

* Value required to support weight, profile and parasite drags for single wing beat.

opportunity to measure the properties of the vortices in comparison with theoretical descriptions of flight performance.

Model predictions of wake parameters and induced power for the morphological and kinematic data of Table 1 are shown in Table 3, together with measured values. As the bird is flying very slowly, parasite and profile drags are small compared with weight: equivalent flat plate area of the body is estimated as $1.42 \times 10^{-3} \text{ m}^2$ so that parasite drag is $4.9 \times 10^{-3} \text{ N}$, while the horizontal component of profile drag is estimated as $1.3 \times 10^{-2} \text{ N}$ if profile drag coefficient is 0.02 (cf. Rayner, 1979a). These drag forces are negligible compared with weight $Mg = 3.43 \text{ N}$, even allowing for substantially higher drag coefficients than quoted, and therefore the wake momentum angle ψ (to the vertical Z axis) should be small (0.30°). Measured angles range between 8.0° and 13.5° , and the increase in angle is largely the result of 'solid-body' rotation of the vortex ring induced by vorticity generated by previous wing strokes; such rotation can be readily distinguished on many of the photographs obtained.

The form of the vortex-ring model used to predict the wake configuration is essentially that described in detail by Rayner (1979a), but with certain simplifications incorporated, partly as a response to these experiments. Profile drag and power are now calculated by blade-element methods for the upstroke as well as for the downstroke, but since at this flight speed profile drag is insignificant, the change is not critical. The more important change is possible because wing-beat kinematics have been determined from film in parallel with flow visualizations. In its original form the model included a two-dimensional equilibrium condition expressing the balance of mean forces in horizontal and vertical planes: this condition fixed the vortex-ring momentum angle and vortex momentum, and imposed a constraint on wing-beat kinematics so that the vortex sheet shed by the wings during the downstroke could deform under its self-induced downwash into a vortex ring of the appropriate configuration. It is th

Second constraint that has been relaxed, since with full kinematic data available it would be redundant. Moreover, these experiments indicate that while vortex roll-up does occur, at these speeds at least it is a more complex process than originally envisaged, and, pending further experimental evidence, it is unjustified to include a description of vortex development in the model. The condition now takes the less strict form of a constraint on wing-beat geometry, in that the mean angle of wing-tip travel to the horizontal (ψ_1) must be greater than the momentum angle ψ . Since here ψ_1 is approximately 45° there is no difficulty: the constraint only becomes important in fast flight, where it imposes an upper limit on flight speed. As speed increases ψ_1 falls, whereas ψ rises as profile and parasite drags become bigger; beyond a certain speed the wing beat cannot generate sufficient thrust. It is not known whether this constraint is more critical than that of obtaining sufficient power output.

As explained above, ring convection velocity and self-energy are calculated on the basis of constant vorticity across the vortex core, so that $\bar{A} = 0.25$. Predicted self-energy is calculated for the elliptic vortex ring by the formulae given by Rayner (1979a, equations 42 and 43), while measured self-energy is obtained for the equivalent circular ring using equation (9); if the observed ring is assumed to be elliptical then it has very low eccentricity, and the exact elliptical self-energy is close to the value given in Table 3.

DISCUSSION

Theory and experiment compared

It is immediately apparent from Table 3 that the vortex rings measured in the wake are significantly different from expected; they are smaller, and also have lower circulation, and therefore the momentum convected into the wake with each ring is substantially lower than expected, being only 60 % of that required to support the bird's weight. (The momentum associated with a vortex ring is given by its vector area times the circulation times the fluid density). Even allowing for the rough-and-ready nature of some of the calculation, the size of the measured wake momentum deficit is disturbing. Apparently the reaction force from air accelerated into the wake by aerofoil action of the wings is only about three-fifths of that required for weight support.

Primarily because of the size and strength discrepancy, the estimated ring self-energy $E_s = 0.76$ J is also 60 % of predicted (1.29 J). If we calculated induced power P_i as E_s/T as explained above, then P_i is only 5.05 W, a surprisingly low value for a bird of this size at this flight speed. This estimate should not, however, be seen as fully reliable until the momentum deficit has been satisfactorily explained.

The wake element spacings and ring convection velocities also differ from prediction, due in part to the different size and strength of the measured ring: however, the equivalent circular ring to that measured would travel at 2.43 m s^{-1} if isolated, and it is unlikely that vortex interactions would reduce this to as low as 1.72 m s^{-1} . It is feasible that this discrepancy is diagnostic of misinterpretation of the nature of the vortex field, but in view of the regularity with which near-planar, near-circular vortex loops were discerned this appears to be unlikely.

Inspection of equation (9) shows that the critical quantities affecting estimation of E_s , and hence P_i , are circulation K and ring radius R . All other quantities including

the core radius R_0 and the constant \bar{A} are the same in both cases. The predicted and measured circulations do not differ appreciably, and the root of the discrepancy in momentum and induced power calculations appears to lie in the value of R measured from the photographs.

Before taking the comparison of results any further, it is worth summarizing the assumptions made in each case and considering their effects on the outcome. As explained above, calculation for the vortex ring model is based on the premise that forces on the bird are balanced: it follows that the momentum of each vortex ring must balance the bird's weight, together with the vector sum of profile and parasite drags, for the duration T of each wing-beat. Ring geometry is calculated from wing-beat kinematics by assuming near-elliptical loading distribution on the wing during the down-stroke, and effectively no loading during the upstroke. Momentum balance determines the circulation of the wake vortex, and wake energy and induced power are computed. Momentum balance is thus an inviolable condition, vital to the model calculations, but it is hard to see how the condition, derived directly from Newton's second law of motion, can be relaxed if the bird is in steady level flight.

At this very low flight speed the bird must be experiencing the most demanding of all flight conditions, having to generate virtually all wing force by the wing-beat alone as there is relatively little forward air speed. It is to be expected, therefore, that this flight pattern will present the vortex-ring model with its most strenuous test. One outcome of the experiments which is not surprising is that the rings are rather smaller than expected; ring size is determined by loading distribution on the wing, and clearly this is somewhat less favourable than the assumed near-elliptical distribution. To compensate, the circulation should be much higher (approx. $3.28 \text{ m}^2 \text{ s}^{-1}$) for these small rings to support the weight, but evidently this is not the case.

No momentum balance condition of course is either assumed or stipulated in the direct computation of momentum from ring size and circulation or of self-energy E_s from equation (9). Here, the approximation is valid for circular, planar, small cored-vortex rings where $R_0 < 0.25 R$ (Norbury, 1973). The latter condition is satisfied but the rings are not circular, and we cannot claim to have shown that they are truly planar. The small departures from circular shape do not affect ring energy, but departures from planarity may cause a small increase. The model also includes the interactive energy of successive rings in the wake. The magnitude of this is assumed to be small, as is indicated by the wake photographs; it is estimated for the predicted wake as 0.14 J , approximately 10% of the estimated self-energy, and accordingly has been ignored. Induced power is likely therefore to have been slightly underestimated, but it will suffice as a first approximation at the rate of energy flow in the wake. In view of the as yet unexplained momentum deficiency, we are not in a position to argue whether this represents the true induced power demanded from the bird.

Vortex dynamics

The nature and magnitude of the wake momentum deficit imply that there is a conceptual flaw in the vortex ring theory, or the measurements, or both. In both cases, it is assumed that the deformed, unstable, vortex sheet initially shed from the wingtips and trailing edges rolls up into a vortex ring without loss of momentum. This argument is subject to certain modifications and qualifications to allow for the effects of viscosity.

Maxworthy (1974) has described the formation and motion of turbulent vortex rings in the Reynolds number ($Re = 2RU_s/\nu$; ν is the kinematic viscosity) range $0.25 \times 10^4 - 0.75 \times 10^4$; similarly defined, $Re = 3.4 \times 10^4$ for our rings in the wake. Two fundamental processes were identified as entrainment and subsequent rejection of fluid into a turbulent wake, and the resulting decrease in ring impulse as vorticity is deposited into the wake appears as a momentum deficit therein. Maxworthy (1977) also described an axial flow along the core of a turbulent vortex ring; such an axial component can be detected in photographs like Fig. 4, and Widnall, Bliss & Zalay (1971) have remarked that a radial force would be necessary to support a momentum flux around a vortex ring. While noting these considerations, it is difficult to make valid comparisons when the generation mechanisms of the vortex flows are so different. We may further note that the azimuthal wave propagation described by Maxworthy took place about 10 ring diameters downstream of the generating nozzle and therefore far beyond the range we are considering, and also that there is no obvious large scale turbulent structure aside from the vortex ring visible in our photographs.

Similarly, viscous dissipation of the ring energy and observable wake momentum has been ignored. This is justified, according to Saffman (1970) for $t \ll R^2/\nu$ where t is a suitable time scale, ν is the kinematic viscosity of the fluid and R is the ring radius. In our case, $\nu = 0.15 \times 10^{-4} \text{ m}^2 \text{ s}^{-1}$ and $R \approx 0.2 \text{ m}$, so that viscous decay of the ring is not critical within $2.7 \times 10^3 \text{ s}$, rather more than the stroke period 0.15 s .

It seems unlikely then that these turbulent and viscous effects will modify the flow field to anything like the extent required to explain the measured wake momentum deficit. Neither can we identify any other large scale structures in the wake which could account for the missing momentum. For example, a flow normal to the tail surface can be seen towards the end of the downstroke, just after depression of the tail, but the vertical component of the reaction force is estimated to be less than 10 % of that required.

$\underline{D}_{\text{par}}$ and $\underline{D}_{\text{pro}}$ should contribute little towards the overall lift at these low flight speeds. Furthermore, a significant contribution towards weight support from $\underline{D}_{\text{pro}}$, for example, would be accompanied by a concomitant increase in the drag which would, in turn, have to be compensated by increasing the vortex wake momentum. The energy expended against $\underline{D}_{\text{par}}$ and $\underline{D}_{\text{pro}}$ is assumed to pass into a separate viscous wake and there is no evidence from the photographs to suggest that such a wake might contain the required momentum.

CONCLUSION

The measured wake momentum deficit appears to imply a physical impossibility and it is difficult to identify possible sources of error. Indeed we are in no position to state categorically that the deficiency actually exists. Similarly, we cannot claim to have made a true measurement of P_i and we must remain equivocal concerning the accuracy of the various theoretical estimates of P_i .

As guidance for future attempts to resolve this paradox, we might bear in mind the fact that the conceptual model used in the measurements bears many similarities and shares many of the assumptions of the model which we are attempting to test. Also, the crucial importance of accurate measurements of the ring radius, R and, to a lesser

extent the circulation, K , has been highlighted by the somewhat puzzling results presented here and these quantities should be very carefully measured in the further work which seems to be necessary.

Special thanks are due to Professor R. T. Severn of the Department of Civil Engineering and Professor B. K. Follet of the Department of Zoology for their support and advice at critical stages of this research. We would also like to thank Dr K. D. Scholey for his assistance in ciné-film analysis and Mr G. Gooding at the University Computer Centre, Bristol for his noble efforts on our behalf. The financial support of the Science and Engineering Research Council is gratefully acknowledged.

REFERENCES

- BATCHELOR, G. K. (1967). *An Introduction to Fluid Dynamics*. Cambridge: Cambridge University Press.
- DIDDEN, N. (1977). Untersuchung laminarer, instabiler Ringwirbel mittels Laser – Doppler – Anemometrie. *Mitt. MPI Stromungsforschung AVA*, Nr. 64, Göttingen.
- FAIG, W. (1973). Model deformations due to radial lens distortion. *Civil Engineering Studies*, Photogrammetry Series No. 26, University of Illinois, Urbana, Illinois.
- FRAENKEL, L. E. (1970). On steady vortex rings of small cross-section in an ideal fluid. *Proc. R. Soc. A* **316**, 29–62.
- GÜHLER, M. & SALLET, D. W. (1979). The formation of vortex rings and their initial motion. *Z. Flugwiss.* **2**, 109–115.
- HALLERT, B. (1960). *Photogrammetry*. London: McGraw-Hill.
- INGHILLERI, G. (1968). A treatise on analytical photogrammetry. (Lecture Notes). *Civil Engineering Studies*, Photogrammetry Series No. 10, University of Illinois, Urbana, Illinois.
- KARARA, H. M. (1980). Non-metric cameras. In *Developments in Close-Range Photogrammetry*, (ed. K. B. Atkinson). London: Applied Science Publishers Ltd.
- KARARA, H. M. & FAIG, W. (1980). An exposé on photographic data acquisition systems in close-range photogrammetry. *International Archives of Photogrammetry* **23**, 402–418.
- KOKSHAYSKY, N. V. (1979). Tracing the wake of a flying bird. *Nature, Lond.* **279**, 146–148.
- LEE, R. E. (1976). Helium bubble flow visualization system. Unpublished Report. Department of Engineering Science, University of Exeter.
- LIGHTHILL, M. J. (1973). On the Weis-Fogh mechanism of lift generation. *J. Fluid Mech.* **60**, 1–17.
- MAGNAN, A., PERRILLIAT-BOTONET, C. & GIRERD, H. (1938). Essais d'enregistrements cinématographiques simultanés dans trois directions perpendiculaires deux à deux de l'écoulement de l'air autour d'un oiseau en vol. *C.r. hebd. Séanc. Acad. Sci. Paris* **206**, 462–467.
- MAXWORTHY, T. (1974). Turbulent vortex rings. *J. Fluid Mech.* **64**, 227–239.
- MAXWORTHY, T. (1977). Some experimental studies of vortex rings. *J. Fluid Mech.* **81**, 465–495.
- NORBURY, J. (1973). A Family of steady vortex rings. *J. Fluid Mech.* **57**, 417–431.
- PENNYCUICK, C. J. (1975). Mechanics of flight. In *Avian Biology*, Vol. 5, (eds D. S. Farner, J. R. King & K. C. Parkes). London: Academic Press.
- RAYNER, J. M. V. (1979a). A vortex theory of animal flight. II. The forward flight of birds. *J. Fluid Mech.* **91**, 731–763.
- RAYNER, J. M. V. (1979b). A new approach to animal flight mechanics. *J. exp. Biol.* **80**, 17–54.
- SAFFMAN, P. G. (1970). The velocity of viscous vortex rings. *S.I.A.M. JI* **49**, 371–380.
- SALLET, D. W. & WIDMAYER, R. S. (1974). An experimental investigation of laminar and turbulent vortex rings in air. *Z. Flugwiss.* **22**, 207–215.
- SULLIVAN, J. P., WIDNALL, S. E. & EZEKIEL, S. (1973). Study of vortex rings using a laser doppler velocimeter. *AIAA Journal* **11**, 1384–1389.
- THOMPSON, M. M. (1966). (ed). *Manual of Photogrammetry*, 3rd edition. American Society of Photogrammetry, Falls Church, VA.
- TUCKER, V. A. (1973). Bird metabolism during flight: evaluation of a theory. *J. exp. Biol.* **58**, 689–709.
- WIDNALL, S. E., BLISS, D. & ZALAY, A. (1971). Theoretical and experimental study of the stability of a vortex pair. In *Aircraft Wake Turbulence and its Detection*; Proceedings of the Symposium, Seattle, Washington, pp. 305–338.
- WOLF, P. R. (1974). *Elements of Photogrammetry*. New York: McGraw-Hill.